Adaptive optics fluorescence lifetime imaging ophthalmoscopy of *in vivo* human retinal pigment epithelium

JANET A. H. TANG,[1,2,5,*] **CHARLES E. GRANGER,**[1,2,5] **KARTEEK KUNALA,**[2] **KEITH PARKINS,**[2] **KHANG T. HUYNH,**[2,3] **KRISTEN BOWLES-JOHNSON,**[2,4] **QIANG YANG,**[2] **AND JENNIFER J. HUNTER**[1,2,3,4]

[1]*The Institute of Optics, University of Rochester, Rochester, NY 14627, USA*
[2]*Center for Visual Science, University of Rochester, Rochester, NY 14627, USA*
[3]*Department of Biomedical Engineering, University of Rochester, Rochester, NY 14627, USA*
[4]*Flaum Eye Institute, University of Rochester, Rochester, NY 14627, USA*
[5]*Contributed equally*
[*]*jhrdina@ur.rochester.edu*

Abstract: The intrinsic fluorescence properties of lipofuscin – naturally occurring granules that accumulate in the retinal pigment epithelium – are a potential biomarker for the health of the eye. A new modality is described here which combines adaptive optics technology with fluorescence lifetime detection, allowing for the investigation of functional and compositional differences within the eye and between subjects. This new adaptive optics fluorescence lifetime imaging ophthalmoscope was demonstrated in 6 subjects. Repeated measurements between visits had a minimum intraclass correlation coefficient of 0.59 Although the light levels were well below maximum permissible exposures, the safety of the imaging paradigm was tested using clinical measures; no concerns were raised. This new technology allows for *in vivo* adaptive optics fluorescence lifetime imaging of the human RPE mosaic.

1. Introduction

The retinal pigment epithelium (RPE) is the densely packed monolayer of cells between the photoreceptors and the choroid that protects and supports the retina. The RPE recycles retinoids in the visual cycle [1], performs phagocytosis of photoreceptor outer segments, diffuses oxygen and nutrients to the photoreceptors, and exports metabolic waste products into the bloodstream [2,3]. The health of the RPE is related to the health of the retina; RPE degeneration is a key feature in diseases such as Stargardt disease [4,5], retinitis pigmentosa [6,7], and age-related macular degeneration (AMD) [8,9]. *In vivo* adaptive optics images of the RPE mosaic have been used to detect and monitor diseases [4,10,11], typically by utilizing the autofluorescence of lipofuscin and other lysosome-related granules [11–14]. Lipofuscin specifically would be beneficial to characterize and track *in vivo* because, although it accumulates with age [15] as a by-product of phagocytosis [16,17], it can increase more rapidly with disease [4,18] leading to toxicity to the RPE and eventually to photoreceptor dysfunction and death [19,20]. The ability to quantify the compositional and functional properties of lipofuscin and the RPE cells *in vivo* could lead to a better understanding of the mechanisms and progression of disease before structural changes occur as well as provide an assessment of the efficacy of therapies at the cellular level [8,21].

Several methods to quantitatively image the RPE include fluorescence intensity, fluorescence spectra, and fluorescence lifetime. While changes in disease have been tracked with fluorescence intensity in adaptive optics scanning light ophthalmoscopes (AOSLO) [4,11], measurements of

absolute fluorescence intensity (quantitative fluorescence) between subjects and even between days, are difficult in AOSLO and can vary day-to-day due to changes in the quality of the adaptive optics correction and the subject's tear film, positioning of the subject, stability of the imaging sources, etc. [22] Separating the contributions from multiple fluorophores can also be complicated in fluorescence intensity as well as fluorescence spectra measurements since many retinal fluorophores have overlapping spectra. On the other hand, fluorescence lifetime – the time from excitation until the fluorescence is decayed to 1/e – is theoretically independent of intensity [23]. Along with careful choice of excitation wavelength, fluorescence lifetime has the potential to characterize relative contributions from multiple fluorophores – even those with overlapping emission spectra because each fluorophore has a characteristic lifetime [24,25]. The exponential decay can be measured at each pixel of an image providing a spatial map of lifetime over the imaging field which allows for the mapping of fluorophore spatial distribution and the measurement of molecular properties, dynamics, and environmental factors [26,27] and has been used to identify diseased retinas [28,29].

Fluorescence lifetime imaging ophthalmoscopy (FLIO) has been implemented in a clinical device and has been used to identify differences between healthy subjects and patients in several diseases including AMD [30] and retinitis pigmentosa [31]; these differences occur both in lifetime magnitude and spatial pattern across the macula. See [29,32,33] for detailed reviews of FLIO. The clinical FLIO does not examine a specific retinal layer but rather measures lifetimes from a volume of the retina. The 473 nm laser currently used in clinical FLIO instruments excites several endogenous retinal fluorophores, including those contained in RPE lipofuscin, flavin adenine dinucleotide (FAD), oxidized melanin [32], and macular pigment [34]. Targeted lifetime analysis is complicated by overlapping fluorescence from these additional fluorophores as well as by fluorescence from the eye's crystalline lens that is not fully rejected by the instrument [35,36]. FLIO may have potential when combined with an AOSLO, where improved axial and lateral resolution could allow cellular-scale lifetime measurements and reduce signal from the lens and other retinal layers, as demonstrated *in vivo* in the mouse and macaque [37,38]. Furthermore, the excitation wavelength and detection bandwidth may be carefully chosen to selectively excite and analyze lipofuscin in the RPE and mitigate macular pigment influence [39,40].

AOFLIO in humans *in vivo* is challenging because of the need to juggle adequate sampling, light safety restrictions, and fast imaging that ensure patient comfort and minimize the effects of saccades on image quality. Furthermore, diseased and aged eyes often have decreased fixation ability and decreased quality of correction due to changes in the monochromatic and chromatic optical qualities of the eye, increased movement, instability of the tear film, and variable quality in the wavefront sensing reflection.

The aim of this paper is to demonstrate for the first time AOFLIO for analysis of the human RPE through single-photon excited short-wavelength autofluorescence (SWAF). This imaging modality could help enhance the interpretation of microscopic structure and potentially provide a rapid means of evaluating cell function and health by analyzing the lifetime signals from lipofuscin and other endogenous fluorophores. Herein, an AOSLO for human imaging is converted to perform AOFLIO. Testing, calibration, and optimization are performed on an optical imitation of the eye and a known fluorophore. Finally, the first AOFLIO data are collected from healthy human eyes.

2.   Methods

2.1.   Human subjects

Six human subjects (24-39 YO) without ocular disease and a refractive error of $< \pm 4D$ sphere were recruited. We obtained written informed consent from all subjects before testing; the study was approved by the University of Rochester Research Subjects Review Board and conducted according to the tenets of the Declaration of Helsinki. Subject demographics can be seen in Table 1.

Table 1. Subject demographics

Subject code	Age	Eye	Sex	Axial length (mm)
NOR053a	31	OD	F	24.07
NOR058a	38	OD	M	23.96
NOR060a	34	OD, OS	M	24.61, 24.48
NOR093a	24	OD	F	22.59
NOR094a	39	OD, OS	F	25.05, 24.94
NOR097a	28	OS	M	23.41

2.2. Human AOFLIO system

A previously-described, custom-built AOSLO [41] was modified to include fluorescent lifetime imaging capabilities. The optical layout of the system is illustrated in Fig. 1.
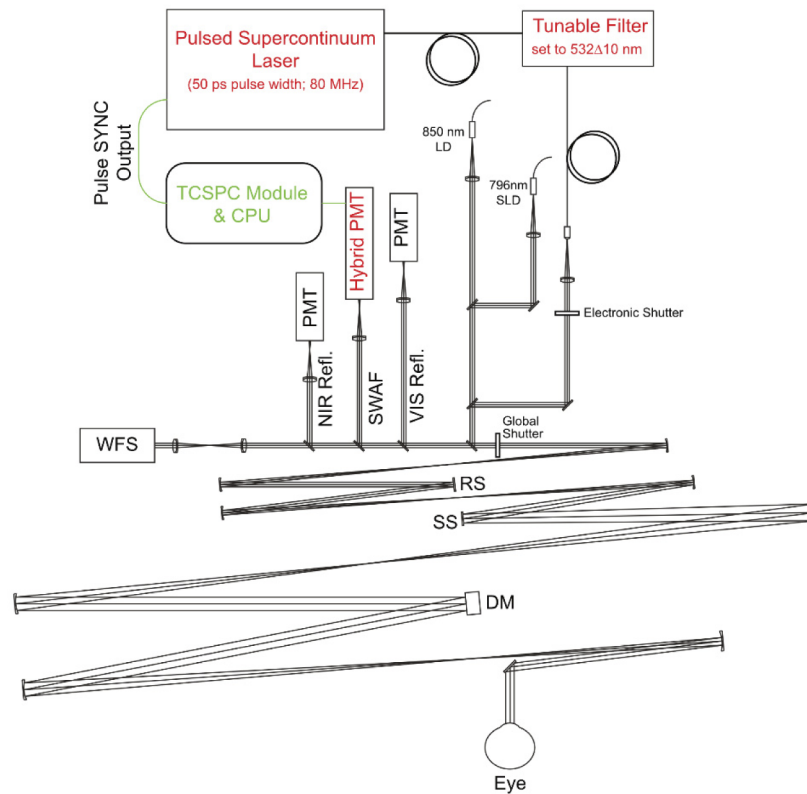

Fig. 1. Custom-built AOFLIO. There are three light sources, an 850 nm source for wavefront sensing, a 796 nm source for navigating around the retina, and a supercontinuum laser source filtered to 532 nm to excite lipofuscin in the RPE. The light was scanned in x and y with a resonant scanner (RS) and a slow scanner (SS). The aberrations of the eye were corrected using a deformable mirror (DM). The 796 nm reflectance and the 532 nm reflectance were imaged on separate PMTs. The 850 nm wavefront sensing light was sent to a Shack-Hartmann wavefront sensor (WFS). The SWAF was detected with a hybrid PMT with a 650/150 nm filter.

A 796 nm superluminescent diode was used for near-infrared (NIR) reflectance images with a 7 mm entrance pupil at the eye. The average power at the cornea was 120–150 µW. The

NIR reflectance channel collected light on a photomultiplier tube (PMT) through a 785/40 nm bandpass filter (MV785/40, Chroma Technology Corp., Bellows Falls, VT) and 1.1 Airy disc diameter (ADD) confocal pinhole. This channel was used for navigation and focus adjustment prior to visible light exposures.

A laser diode with 850 nm center wavelength (QFLD-850-20S-PM, QPhotonics LLC, Ann Arbor, MI) and a 7 mm entrance pupil at the eye was used for wavefront sensing, using ~15 µW average power at the cornea. Reflected 850 nm light from the eye was directed to a lenslet array and CCD camera (ROL-XR-F-M-12-C, QImaging, Surrey, BC) for wavefront sensing. The AOSLO operates in a closed loop with the WFS and deformable mirror (DM-97, ALPAO, Montbonnot-Saint-Martin, FR) through custom software to measure and correct ocular aberrations.

Fluorescence from the RPE was excited with a supercontinuum laser (SuperK EXTREME FIU-15, NKT Photonics, Birkerød, DK) with 10–15 µW power at the cornea and ~50 ps full-width half-max pulse width and an 80 MHz repetition rate, filtered to 532/10 nm (SuperK VARIA, NKT Photononics). The visible light was coupled into the system using a polarization-maintaining fiber (SuperK CONNECT, NKT Photonics). The diameter of the 532 nm beam at entrance pupil of the eye ranged from 3.5-5.5 mm to increase the excitation depth of focus. Visible reflectance was split with a 556 nm short-pass filter (FF556-SDi01-25 × 36, Semrock, Rochester, NY) from the fluorescence signal and imaged through a 525/50 nm bandpass filter (FF03-525/50-25, Semrock) with a 1-2.8 ADD confocal pinhole. This channel provided an image-based indicator of the retinal layer in focus by the excitation source, simultaneously providing feedback of longitudinal chromatic aberration (LCA) compensation accuracy through comparison to the NIR reflectance image.

Fluorescence was captured through a 650/150 nm (575-725 nm) bandpass filter (FF01-650/150-25, Semrock) using a hybrid PMT (HPM-100-40, Becker & Hickl, Berlin, DE); this wavelength range is comparable to the long-spectral channel (LSC) in the clinical FLIO. The fluorescence detector and confocal pinhole were mounted on a motorized 3-axis translation stage for real-time positioning to optimize signal intensity. A larger 3.5 ADD confocal pinhole was used in this channel to increase signal collection and provide tolerance in detector positioning, at the expense of decreased confocality. Image sequences were acquired at 23 Hz frame rate with 576×576 pixels in each frame. A total of 1D of vergence at the eye was induced between the visible and NIR sources to compensate for the LCA of the eye as well as to allow for the focusing of the NIR on the photoreceptors for navigation with the excitation source focused on the fluorescent RPE to maximize fluorescence signal [11]. Additionally, the fluorescence detector was moved along the imaging axis to account for the chromatic aberration between the 532 nm excitation and the 650 nm emission wavelengths. A reference pulse is sent directly from the laser to a commercial time-correlated single photon counting (TCSPC) module (SPC-160, Becker & Hickl, GmbH). The TCSPC works by measuring the time between the reference pulse and when a photon emitted from the sample is received; this measurement is repeated over many excitations to aggregate a histogram of time bins for a single pixel of the image.

Fluorescence lifetime data acquisition was performed using commercial software (SPCM, Becker & Hickl) with 256 time bins. The use of commercial software for fluorescence image acquisition did not allow for real time sinusoidal correction of lifetime images as done on the custom AOSLO acquisition software [42] – desired because of the sinusoidal velocity of the resonant scanner. The lifetime images could not be co-registered and averaged. A combination of eye tracking/optical stabilization [43,44] during data collection and post-processing desinusoiding were utilized to compensate for these deficits and to reduce the number of frames lost due to eye motion during an exposure, improving the signal-to-noise ratio and reducing necessary exposure time.

An initial set of data was taken to test the feasibility of the system followed by a second set taken with improvements to the system – paradigm 1 and 2, respectively. The differences between the two collection paradigms are shown in Table 2. After the first set of images, we added an electronic splitter (HPMCON-02, Becker & Hickl) after the hybrid PMT to allow optimization of the pinhole position to account for each subject's individual LCA as done in Rossi et al. [11]. The addition of the splitter gave us the capability to capture and register a fluorescence intensity image, separate from the SPCM acquisition. Improvements in throughput allowed the pinhole diameter to be reduced to 2.3 ADD for the second set of data. Fluorescence intensity images captured with the splitter through the AOSLO software are called fluorescence intensity images throughout the manuscript; fluorescence intensity images captured through the SPCM software and generated by summing the histograms at each pixel are called AOFLIO intensity images.

Table 2. Two data-collection paradigms

Data paradigm	Field of view	Visible source vergence (D)	SWAF channel pinhole diameter (ADD)	SWAF pinhole position optimization
1	1.75°x1.75° 1.4°x1.4°	-1	3.5	No
2	1.4°x1.4°	-0.8	2.3	Yes

To test the AOFLIO measurement accuracy, a known fluorophore was observed in the model eye. Alexa Fluor 555 (Thermo Fisher Scientific, Inc., Waltham, MA) has a relatively short fluorescence lifetime of 300 ps like that of lipofuscin autofluorescence at similar excitation and emission wavelengths [45–47]. The fluorophore was dissolved in purified Milli-Q water and imaged on a microscope slide placed at the model eye focal plane.

2.3. Imaging protocol

Before subjects were imaged in the AOFLIO system, an infrared reflectance image was obtained as a retinal location reference on the Heidelberg Spectralis HRA (Heidelberg Engineering, Heidelberg, Germany). Axial length was measured in the IOL Master 5 (Zeiss, Jena, Germany) and used to convert degrees across the retina to millimeters. At least 24 hours was allowed between the HRA image acquisition and AOFLIO imaging to avoid overexposure at short wavelengths. 2.5% Phenylephrine and 1% Tropicamide was administered to dilate and cycloplege one eye of each subject. With the other eye occluded, subjects were placed in a headrest with chin and temple mounts and asked to fixate on a dim laser spot visible through a beam splitter. Next, a location was selected. The focus was adjusted to produce the best photoreceptor image in the NIR reflectance channel. For the first paradigm, a sequence of 2–3 short 2 s AOFLIO exposures were recorded at different AO focus settings. The resulting visible reflectance images were examined to determine the sharpest and brightest image, and the system focus was adjusted accordingly. For the second paradigm, the fluorescent channel confocal pinhole position was automatically optimized [11] by sampling the mean pixel value in a series of 5 ms exposures. Finally, 30 s image sequences were collected. The pinhole optimization routine was repeated when image quality decreased, a new location was chosen, or when subjects exited and re-entered the system. In the AOSLO, fluorescence lifetime, visible reflectance, and NIR reflectance were collected simultaneously with a subject's pupil dilated to at least 7 mm.

Following a recording, adjustments to focus, excitation source vergence, or fluorescence detector position were made based on observations of reflectance and fluorescence images. Although focus does not affect the fluorescence lifetime, it does have a strong impact on photon count and cell visibility. Therefore, a second exposure at the same location was often captured after adjusting focus by 0.1D. During image capture, optical tracking was performed using

previously defined protocols [44]; AOFLIO frames where optical tracking failed or residual motion was greater than 15 pixels were removed in post-processing. Imaged retinal locations are listed in Table S1.

2.4. Image analysis

Custom-developed software was used to desinusoid the fluorescence lifetime data for each acquisition using individual look-up tables for sinusoidal rectification [42]. Frames where the optical tracking failed were removed [44]. This software also combined the forward- and backward-scans. The merged, desinusoided fluorescence lifetime data were output as a histogram of photon counts for each pixel in the image.

While not possible for AOFLIO, the 796 nm, 532 nm, and fluorescence intensity from the electronic splitter were strip registered [48], providing residual root-mean-square eye motion of less than 0.2 μm. The fluorescence intensity images in paradigm 2 were coregistered to the 796 nm strip registration using 6 sections to account for TCA changes between the wavelengths throughout the acquisition [12]. Finally, the 6 sections were registered and combined. In its current form, digital registration at the strip-level is not applied to the fluorescence lifetime data. The NIR was averaged across time while the visible reflectance and the fluorescence intensity were summed with time.

Fluorescence lifetimes were determined by fitting an exponential decay to the histogram at each pixel. A single decay curve may have contributions from multiple fluorophores with unique lifetimes, thus a multi-exponential fit was utilized,

$$F(t) = IRF \times F_0 \sum_{k=1}^{n} a_k e^{-t/\tau_k} \tag{1}$$

where F_0 represents the initial fluorescence intensity, n is the number of lifetime components in the fit, and a_k and τ_k are the respective relative abundance and fluorescence lifetime of each component. IRF is the instrument response function – the finite-width response of the imaging system to an infinitely narrow input. For improved lifetime measurement accuracy, the system IRF was measured as described in the supplement and deconvolved by commercial software (SPCImage v8.3, Becker & Hickl) using an iterative fitting process [49]. In addition to the individual component lifetimes, the weighted mean lifetime was evaluated, described as

$$\tau_{mean} = \sum_{k=1}^{n} a_k \tau_k \tag{2}$$

where $\sum_{k=1}^{n} a_k = 1$.

SPCImage was used to fit decay curves, using a nonlinear least-squares fit. Photons from surrounding pixels were included (binned) to increase the photon count. See Fig. S1 for example histograms of binned and unbinned data. Binning increased fit accuracy but reduced the spatial lifetime resolution. The bin was increased until most pixels contained at least 1000 photons – the average number of photons per pixel was 1104 with a maximum of 1880 and minimum of 551 photons in a single histogram after spatial binning and thresholding.; the bin kernel ranged from 11×11 to 17×17 pixels in the first imaging paradigm and was 13×13 pixels in the second – this is equivalent to a kernel size of 9.20 μm. These parameters were derived based on criteria from a previous study that simulated the % error of a_k and τ_k values of a two-component fit with varied time bins and pixel photon counts [50].

The goodness of fit was evaluated with the reduced χ^2 parameter. While lipofuscin fluorescence is known to originate from several bisretinoids [51], we tested the goodness of fit for 2- and 3-components on 3 sample images. This analysis revealed that for a 3-component fit, $a_3 < 5\%$ and gave a marginal improvement to χ^2. Based on those results – tabulated in Table S2 – we used a 2- component fit for the rest of the data. After calculating the decay matrix for the image, arrays were exported with a_k, τ_k, photon count, and χ^2 values for each pixel. A custom MATLAB script

was used to analyze arrays and produce color-mapped fluorescence lifetime images. Colormaps were generated with blue as short lifetimes and red as long which is typical in fluorescence lifetime microscopy literature which has a similar spatial scale as this work; this color scale is the opposite of clinical FLIO reports.

Fluorescence signal and lifetime fit accuracy can be greatly improved by integrating photons and lifetime data from forward- and backward-scan frames in post-processing. Data consistencies between scan directions were first evaluated to ensure lifetime measurements were not skewed by the integration. Eight AOFLIO image sequences from paradigm 1 were desinusoided and separated into forward- and backward-scan data; the structure and average of fluorescence lifetime were compared. The structure of the forward- and backward-scans were similar for the AOFLIO intensity but not for the fluorescence lifetime (Fig. S2). A two-tailed paired t-test was used to compare the averaged fluorescence lifetime data for forward- and backward-scans, where no significant difference was found for the distribution of any of the component lifetimes or relative contributions. Because of this result, forward- and backward-scans were integrated for all AOFLIO data prior to lifetime analysis, with the hopes that the increased photon count of the merged data would likewise improve the lifetime fit accuracy.

To compare on a larger spatial scale, mean values of a_1, τ_1, τ_2, and τ_m were calculated across each image. To test repeatability, overlapping areas were found by aligning unregistered 796 nm reflectance images and cropping the AOFLIO data to the common area in 13 locations in 4 subjects. The intraclass correlation was calculated for AOFLIO parameters at the same location across multiple visits; the repeat visits were at least 6 days apart and at most 3 months apart.

Phasor analysis was also conducted in conjunction with the exponential fitting. The raw decay curves and the shifted and scaled IRF were extracted from the SPCImage software and input into custom MATLAB script. The discrete Fourier transform of each pixel was calculated and evaluated at the repetition frequency of the laser. The imaginary component is the s-axis and the real component the g-axis. This is shown in Eqs. (3) and (4).

$$s_{i,j} = \frac{\sum_{t=0}^{n} d_{i,j}[t] \sin(2\pi t f_{laser})}{\sum_{t=0}^{n} d_{i,j}[t]} \tag{3}$$

$$g_{i,j} = \frac{\sum_{t=0}^{n} d_{i,j}[t] \cos(2\pi t f_{laser})}{\sum_{t=0}^{n} d_{i,j}[t]} \tag{4}$$

where $d[t]$ is the histogram at pixel i, j, and f_{laser} is the laser pulse repetition frequency. Each pixel's histogram results in a data point on the phasor plot. The s and g coordinates can be averaged across an image and across a subject.

2.5. Safety analysis

During imaging, the power incident on the cornea for the three sources (796 nm, 850 nm, and 532 nm) was in accordance with the ANSI Z136.1-2014 standard [52]. Maximum permissible exposures (MPE) were calculated at the smallest imaging field of 1.4×1.4 degrees; the three wavelengths together are using 9.56% of the ANSI thermal MPE; the visible light is using 0.69% of the ANSI photochemical MPE. The average power at the pupil was measured and adjusted before each imaging session. Visible light exposure was controlled with a mechanical shutter and was only incident on the eye during image acquisition and signal optimization.

The reduction of blue autofluorescence (BAF) was quantified as an indicator of retinal damage [53,54]. BAF (λ_{ex}=488 nm; λ_{em} >510 nm), IR reflectance (λ=815 nm), visible reflectance (red free; λ=488 nm), and OCT were captured in the Heidelberg Spectralis HRA + OCT (Heidelberg Engineering, Heidelberg, Germany) before AOFLIO imaging and at least a couple days and up to 3 months after AOFLIO imaging. Imaged locations were determined and normalized using

nearby areas with the same pixel count as described in Masella et al. [55]. The ratio of after and before was determined in 19 locations in 3 subjects as shown in Eq. (5).

$$BAF\ ratio = \frac{I_{after}/N_{after}}{I_{before}/N_{before}} \tag{5}$$

where I is the imaged area and N is the normalization factor from a nearby pixel-matched area. If the ratio is below 1, the retina is potentially being affected by the imaging. A one-sample t-test was conducted to determine if the BAF ratio was significantly different from 1. In addition, OCT and fundus images were qualitatively inspected for changes before and after imaging.

3. Results

3.1. Alexa fluorophore 555

The fluorescence lifetime image of Alexa Fluor 555 dissolved in an aqueous solution had no structure, as expected. The best fit of lifetime data was achieved with a single exponential. The mean lifetime across the image was 300.6 ± 10.2 ps, in excellent agreement with the lifetime reported by the manufacturer. Individual pixels ranged between 250–350 ps.

3.2. Fluorescence lifetime images and lifetime measurements in humans

RPE cells are visible in the fluorescence intensity images (Fig. 2(a),(d)) that were captured using paradigm 2 through the AOSLO acquisition software and registered using the simultaneously obtained IR reflectance video. The fluorescence data captured through the fluorescence lifetime software is desinusoided, but not registered. Because of eye motion, the fluorescence lifetime is blurred as depicted by the corresponding AOFLIO intensity images (Fig. 2(b)) and RPE cells are only occasionally visible (Fig. 2(e)). The average residual eye motion after the frames where tracking failed were removed was 3.97 ± 2.33 pixels. This does not account for TCA compensation between the IR reflectance and visible excitation. The magnitude of mean uncorrected motion is comparable to an error in pixel assignment on the order of 0.08 pixels in clinical FLIO. For each location, the fluorescence lifetime fluctuated on a small spatial scale (Fig. 2(c),(f)). The presence of blood vessels in the fluorescence intensity images appears as a dark line (Fig. 2(d),(e)); a corresponding shift of the fluorescence lifetime at the location of the blood vessel can be seen in Fig. 2(f). Imaging in the first paradigm found that the 0.1D focus adjustments had a strong impact on the photon count; the second paradigm revealed that cell visibility was sensitive to focus separate from photon count. The second imaging paradigm has an increase in the proportion of images with visible RPE likely due to both the ability to account for individual variations in LCA by the addition of the custom splitter electronics and a more even distribution of the vergence between the IR and fluorescence channels – resulting in fewer aberrations in the 532 nm channel.

Comparing the images from similar eccentricities in two different subjects showed a similar fluorescence lifetime range. For the two images shown in Fig. 2, the mean of each distribution of τ_m for all pixels in the image differed 5.50 ps (Fig. 2(i)). The phasor plot shows a shift between the two sample locations (Fig. 2(g),(h),(h')). Figure 3 shows a violin plot for all 6 subjects in this study for τ_m, τ_1, τ_2, and a_1 where the mean of each image at a single location is a single data point; the 38 YO subject has one datapoint because the other locations imaged had an insufficient number of photons for an accurate exponential fit. Figure 4 is a phasor plot with the mean $(g, s) \pm$ standard deviation across all locations for each subject. The phasor locations are closely clustered and show very small variations across subjects. There is insufficient statistical power to permit comparison of parameters across subjects or as a function of eccentricity. The summarized data across all eccentricities for each subject is shown in Table 3. A complete list of data is provided in Table S1.
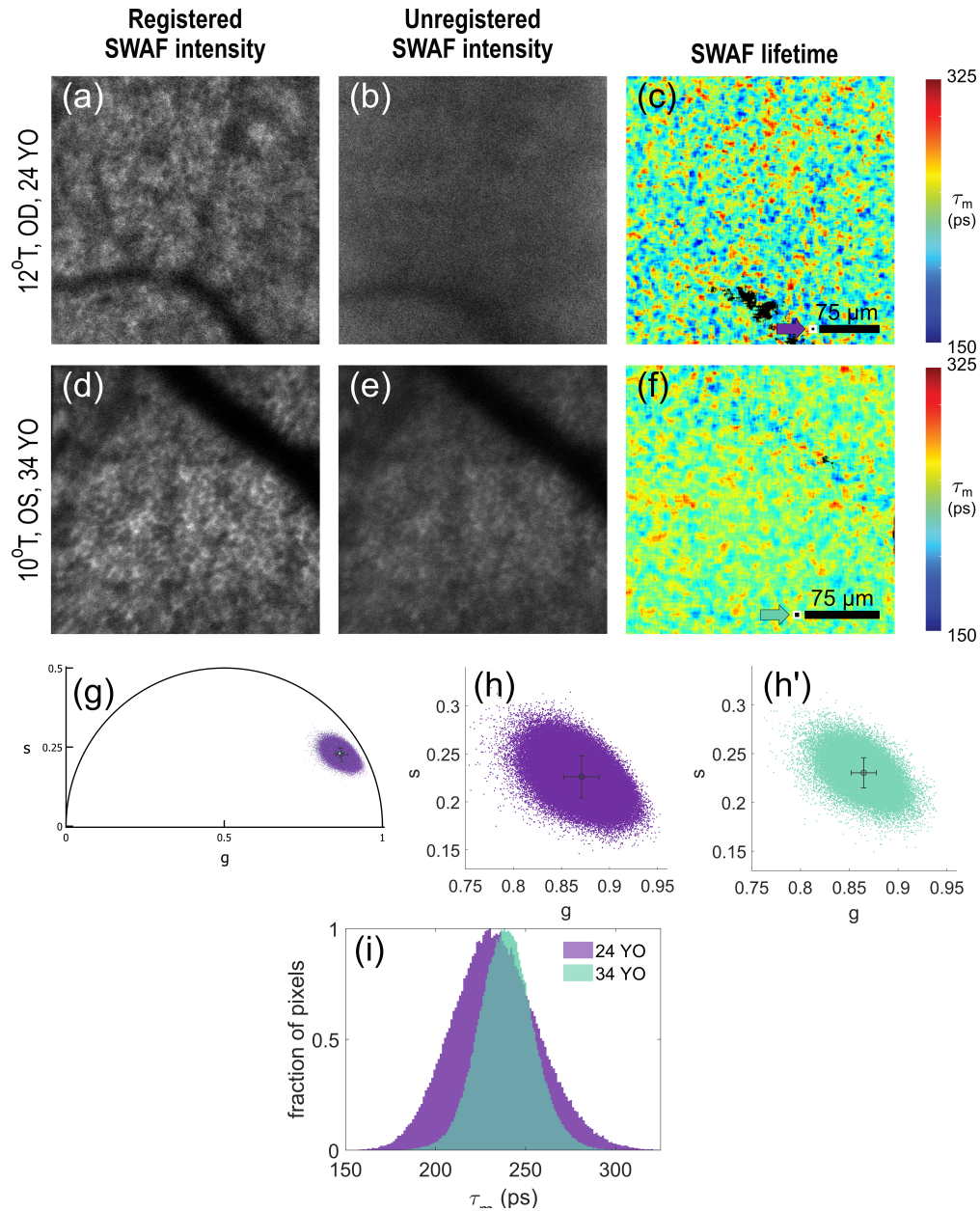
Fig. 2. Representative data in 2 subjects at a similar eccentricity. (a) and (d) show the registered fluorescence intensity from the splitter, (b) and (e) show the unregistered, summed fluorescence intensity from the splitter and (c) and (f) show the fluorescence lifetime. (a), (b), and (c) are from the same image sequence for the 24 YO while (d), (e), and (f) are from the same image sequence for the 34 YO. (g) shows the phasor plot for the 2 subjects with each point showing a binned pixel in the image; the mean and standard deviation are shown. (h) and (h') show a zoomed-in phasor plot for the 24 YO and 34 YO, respectively. (i) shows the histogram of the two images for each subject. The black box indicated by the arrow near the scalebar in (c) and (f) is the binning size of 13×13 pixels used for processing.
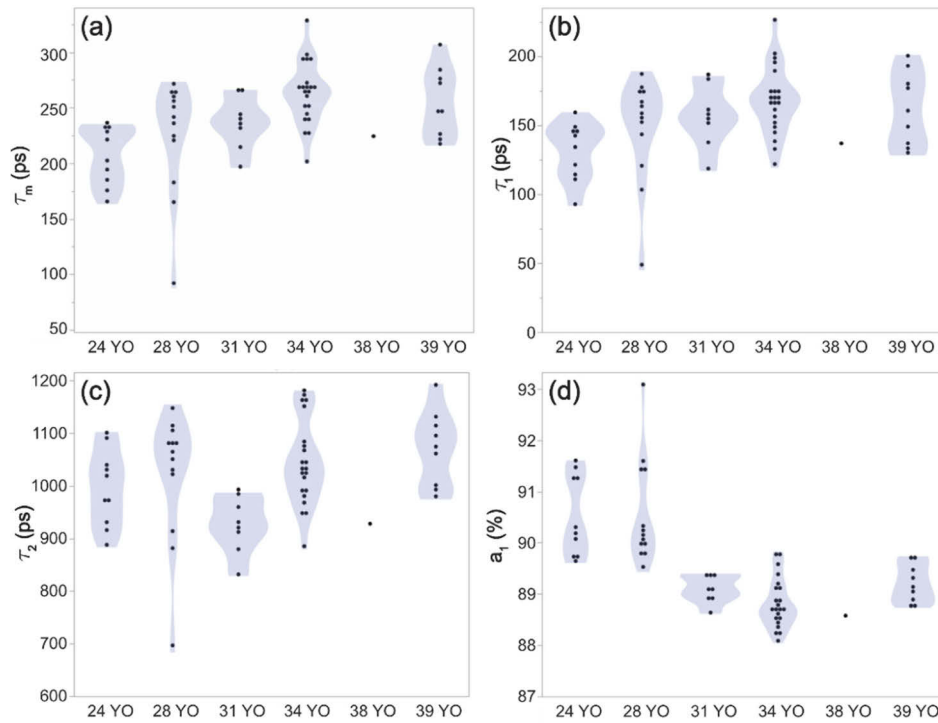
Fig. 3. (a) shows a violin plot of the data for τ_m for all subjects. The data for τ_1, τ_2, and a_1 are shown in parts (b), (c), and (d), respectively.
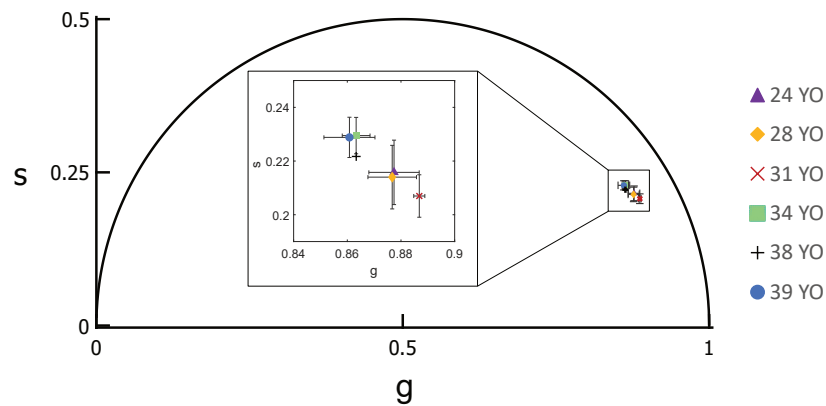

Fig. 4. The phasor plot across subjects. Each data point represents one subject. The error bars are the standard deviation across all locations in that subject. The inset shows a zoomed-in version of the data.

3.2.1. Lifetime measurement repeatability at the same location

While the AOFLIO intensity pattern is repeatable between the forward- and backward-scans, the lifetime map comparison of forward- and backward-scan data is not remarkably similar in the spatial pattern (Fig. S2).

Table 3. the average data for each subject across all eccentricities

	τ_m (ps)	τ_1 (ps)	τ_2 (ps)	a_1 (%)	g	s	Data paradigm
NOR093 (24 YO)	206.8 ± 23.3	130.9 ± 18.9	994.4 ± 65.8	90.5 ± 0.7	0.88 ± 0.01	0.22 ± 0.01	2
NOR097 (28 YO)	227.3 ± 47.9	149.7 ± 35.5	1027.1 ± 115.9	90.5 ± 1.0	0.88 ± 0.01	0.21 ± 0.01	2
NOR053 (31 YO)	236.7 ± 23.4	156.2 ± 22.0	926.0 ± 52.9	89.1 ± 0.3	0.89 ± 0.00	0.21 ± 0.01	1
NOR060 (34 YO)	263.0 ± 27.4	168.2 ± 23.8	1044.7 ± 79.3	88.8 ± 0.5	0.86 ± 0.01	0.23 ± 0.01	1 & 2
NOR058 (38 YO)	224.5	136.9	928.3	88.6	0.86	0.22	1
NOR094 (39 YO)	255.3 ± 29.2	161.8 ± 25.3	1071.2 ± 67.4	89.2 ± 0.3	0.86 ± 0.01	0.23 ± 0.01	2
Across subjects	240.9 ± 38.1	155.1 ± 29.0	1019.7 ± 92.7	89.6 ± 1.0	0.87 ± 0.01	0.22 ± 0.01	

Figure 5 shows example images from one repeated location in a 39 YO subject. The fluorescence intensity shows that the same location was imaged with repeated hypo- and hyper-fluorescent regions (Fig. 5(a),(b),(d),(e)). The fluorescence lifetime, however, does not have the same structure between repeat visits (Fig. 5(c),(f)). The distribution of mean fluorescence lifetime in the histogram shows that while the structure is different between the images, the range of fluorescence lifetime is overlapping (Fig. 5(i)). The phasor plot also shows little difference – the average points for each visit are indistinguishable (Fig. 5(g),(h),(h')). A plot showing the average and standard deviation for each test-retest location is shown in Fig. 6 for τ_m, τ_1, τ_2, a_1, s, and g. Table 4 shows the data between the two visits as well as the intraclass correlation coefficient where 1 represents perfectly correlated data and 0 is uncorrelated data. The lowest intraclass correlation coefficient was found for τ_2 (0.59). The highest intraclass correlation occurred for the g phasor coordinate (0.96).

Table 4. Average data for visit 1 and visit 2 and statistical significance

	Visit 1	Visit 2	Correlation Coefficient
τ_m (ps)	221.11 ± 50.038	228.94 ± 38.91	0.72
τ_1 (ps)	142.12 ± 36.59	148.40 ± 29.78	0.61
τ_2 (ps)	1014.62 ± 119.87	1028.62 ± 80.63	0.59
a_1 (%)	90.36 ± 1.24	90.27 ± 0.73	0.89
(g, s)	$(0.87 \pm 0.01, 0.22 \pm 0.01)$	$(0.87 \pm 0.01, 0.22 \pm 0.01)$	(0.96, 0.86)

3.2.2. AOFLIO safety in humans

To assess the presence of light-induced changes in the RPE, the BAF was calculated. Across 19 locations in 3 subjects, the mean BAF ratio is 1.00 ± 0.06. A one sample t-test revealed that the data was not significantly different from 1 (p = 0.78) indicating that there was no long-term reduction in BAF with AOFLIO imaging. Figure 7 shows HRA images taken before and after AOFLIO for one subject; Fig. 8 shows an OCT cut through the fovea that covers most of the imaged locations. The full OCT scans are provided in Visualization 1, Visualization 2, Visualization 3 and Visualization 4. Qualitative assessment of OCT, IR reflectance, and visible reflectance (red free) showed no impact from AOFLIO.
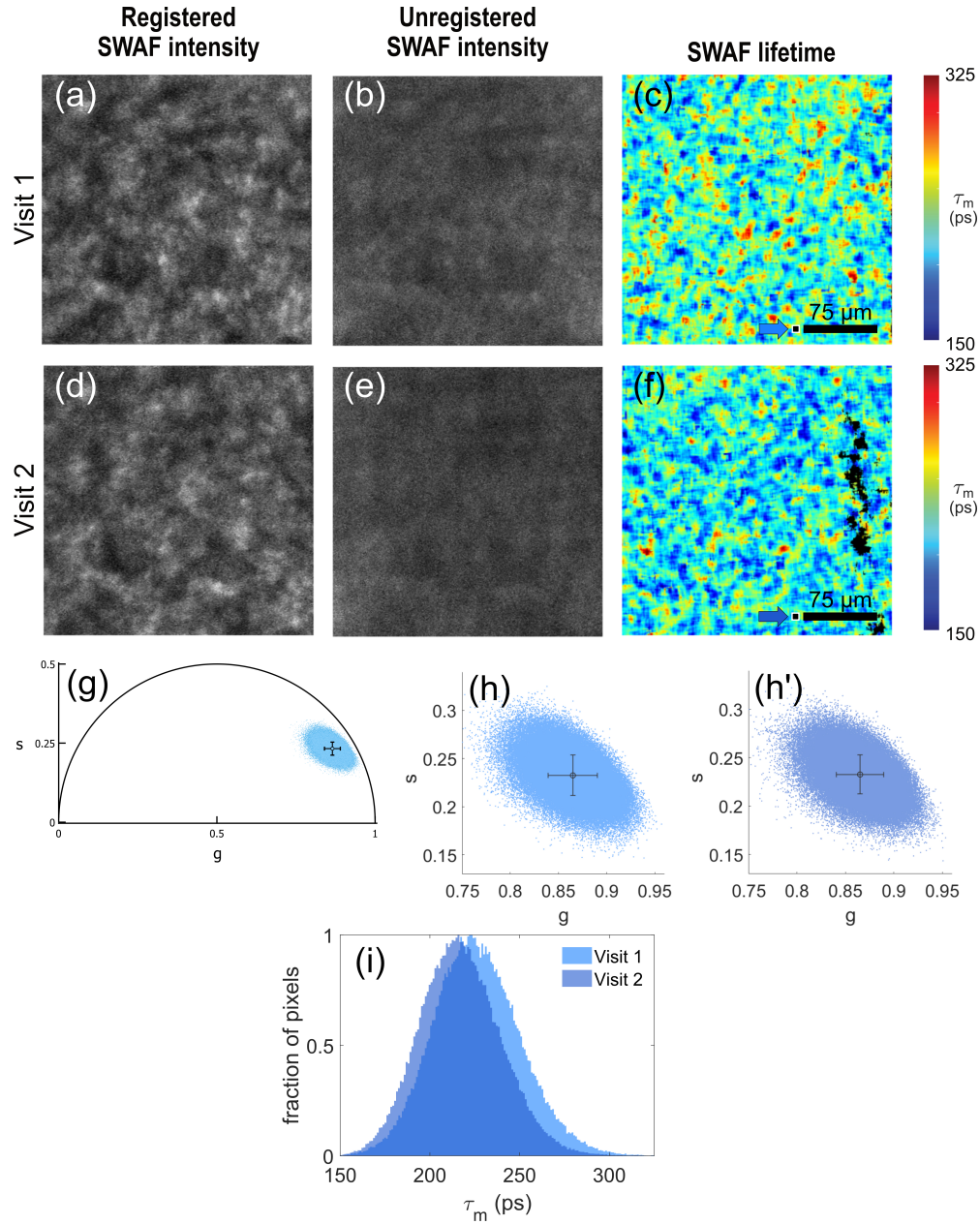
Fig. 5. A sample location (6.6°T, 4° I) repeated in two visits a month apart. Parts (a) and (d) show the registered SWAF intensity from the splitter for visit 1 and 2, respectively. Parts (b) and (e) show the unregistered SWAF intensity from the splitter for visit 1 and visit 2, respectively. Parts (c) and (f) show the SWAF lifetime between visits 1 and 2 with the black box indicated by an arrow near the scalebar showing the bin size of 13×13 pixels. (g) is the phasor plot (h) and (h') are a zoomed-in phasor plot for visit 1 and visit 2, respectively, and (i) is the histogram of τ_m with both visits plotted where each datapoint is pixel in the image. The mean and standard deviation of the phasor data across each image are shown in (g), (h), and (h').
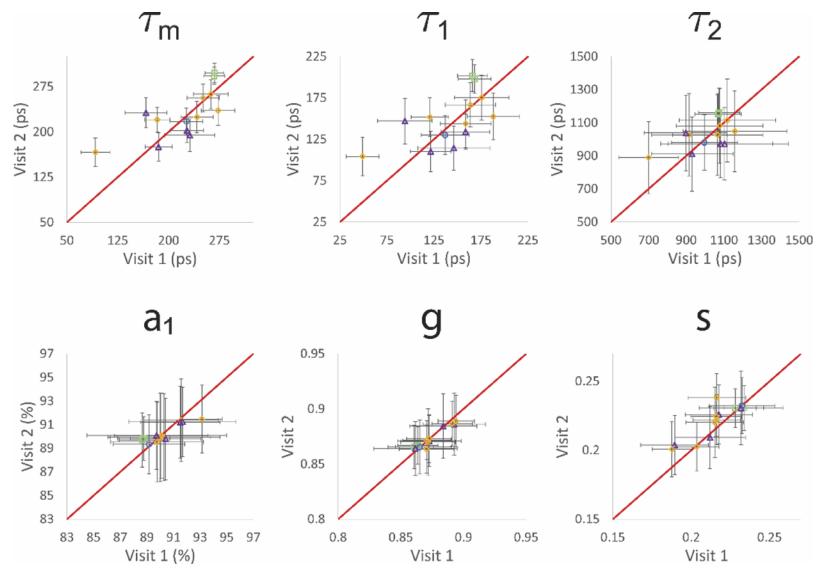
Fig. 6. Visit 2 vs Visit 1 plots for τ_m, τ_1, τ_2, a_1, the phasor s coordinate, and the phasor g coordinate are shown. Each point is the average parameter for an image taken at visit 2 vs the average across an image taken at visit 1 at the same location. The red line is the 1-to-1 line. Error bars represent the standard deviation of the fluorescence lifetime across that image at that location.
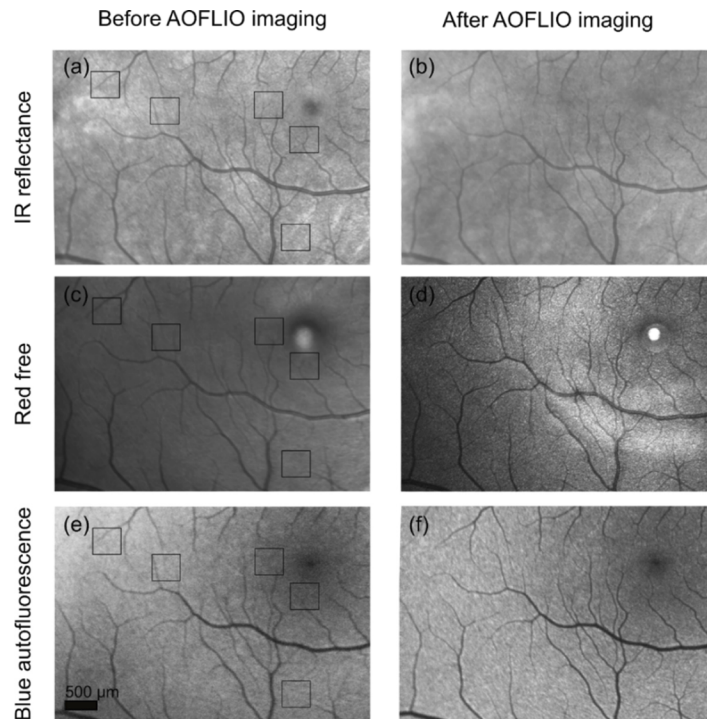

Fig. 7. Images of a subject's retina before and after AOFLIO imaging. The black boxes show the locations of where AOFLIO was imaged. (a) and (b) show IR reflectance images. (c) and (d) show red-free images. (e) and (f) show blue autofluorescence images taken before and over a month after AOFLIO, respectively.
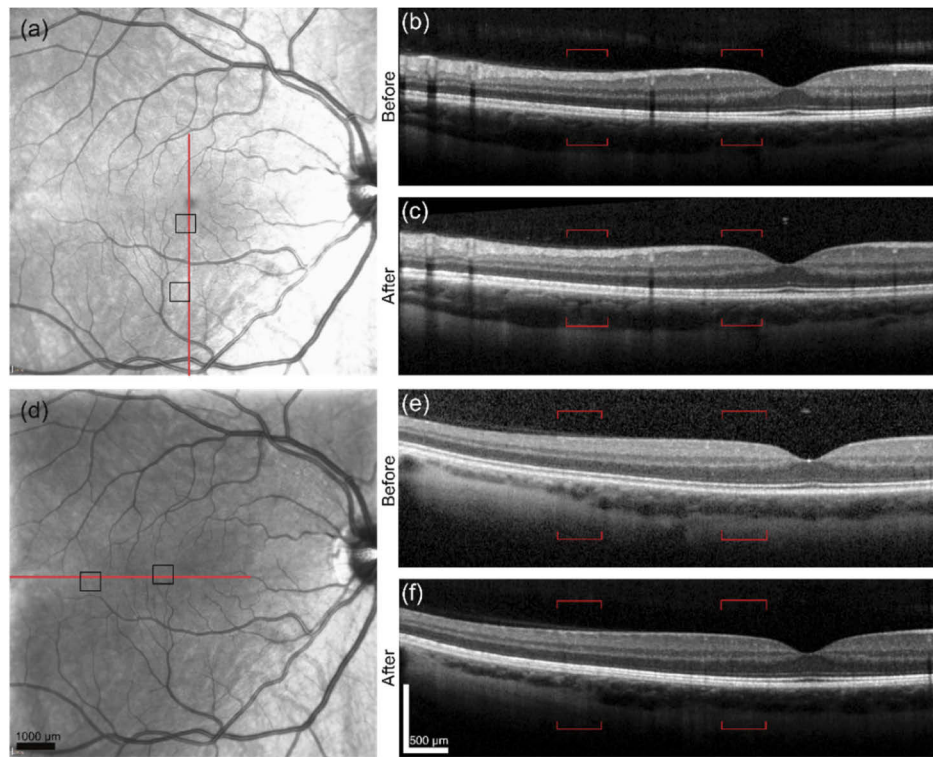
Fig. 8. (a) and (d) show the IR photo with imaged locations in the black box. The red lines are the location of the OCT scans. OCT scans (b), (e) show before and (c),(f) show after AOFLIO imaging. The boxes on the fundus photos correspond with the brackets on the OCT images.

4. Discussion

The work in this paper demonstrates high resolution fluorescence lifetime measurements with SWAF in the living human eye, presenting a new direction for *in vivo* study of the RPE. Fluorescence lifetime analysis is less sensitive to intensity artifacts and often requires less time to analyze in comparison to structural analyses such as cell counting. Even when cellular resolution cannot be achieved, lifetime analysis can still be performed, and with greater lateral resolution than in a clinical FLIO – one pixel in the clinical FLIO is roughly 48 pixels in this study. Using AOFLIO also reduces the effects of lens fluorescence as compared to the clinical FLIO with better axial resolution due to an increase in the confocality of the system. In the latter, the bin size for analysis is 20×20 µm or 30×30 µm [34,56], and the optical resolution in the eye is on the order of 10 µm due to a small beam diameter at the pupil and uncorrected aberrations. For comparison, the bin sizes used in this study were 4–15 µm, and the optical resolution is on the order of 1–2 µm. Although averaging took place across the entire field of view (~408×408 µm), this could be reduced by dividing each image into smaller regions of interest. With efforts to improve fluorescence signal collection and fluorescence lifetime registration, the bin size in AOFLIO can be further reduced, with the goal of eventually allowing analysis at cellular-scale resolution.

While fluorescence lifetime measurements from lipofuscin and the RPE have been reported in several *ex vivo* and *in vivo* studies, results vary widely and are difficult to compare due to variations in preparation and excitation and emission wavelengths. With this in mind, our τ_m

measurements are within the broad range of lipofuscin mean lifetimes (70-1400 ps) reported in the literature [45–47,57–59]. The most similar comparison to the *in vivo* results reported in this paper are from the LSC of clinical FLIO, excited at 473 nm. This is not surprising because we use a similar collection channel and the predominant fluorophore in the LSC is expected to be lipofuscin [45]. The τ_m values in healthy human eyes *in vivo* are reported between 100–150 ps in one study using a 3-component fit [34] and 200–350 ps in another using a 2-component fit [56]. Dysli et al. reported mean lifetimes between ∼275–350 ps for regions between 5−10° eccentricity [56]. Most τ_m measurements in this study, also using a 2-component fit, fall on the short end of that range. However, the clinical study reported an increase in mean lifetime with eccentricity, indicating that clinical measurements could be even longer for most of the locations (>10°) imaged in this study.

The general agreement of lifetime parameters and phasor plot between subjects and imaging sessions is expected considering the similar age and eye-health of the subjects. This corroborates that the system's measurements are repeatable. For clinical FLIO, τ_m in the lipofuscin-attributed LSC channel increases by >100 ps between 20 and 70 years [60]. Between 5° and 10° eccentricity, there is a difference in τ_m of ∼25 ps [56]. With the τ_m standard deviation of 38.14 ps across our subjects, measuring a 25 ps difference with 80% power (probability of avoiding a Type II error) will require 38 measurements per group for each comparison; similarly, to measure a 100 ps difference with 80% power would require 4 subjects for each group. To detect a difference of 25 ps between visits with 80% power, 28 paired visits should be measured. With the currently collected data, there is little to no trend qualitatively with eccentricity or age; future studies with a more expansive subject population will need to be conducted to determine these effects at a 532 nm excitation wavelength. It is unclear, however, if our measures will detect a similar variation with eccentricity as the clinical FLIO because excitation at 532 nm avoids the absorption and excitation of macular pigment.

The lack of repeatability in the fluorescence lifetime structure both between repeat visits and between forward- and backward-scans is likely due to a lack of registration in the lifetime data where eye movements blur the lifetime even with the use of real-time optical tracking; previous studies in our group using AOFLIO in anesthetized macaques show spatial repeatability [38]. The need for registration in fluorescence lifetime data is illustrated in Fig. 2 which shows registered fluorescence intensity images from the splitter with cellular visibility (Fig. 2(a),(d)) and unregistered but desinusoided fluorescence intensity images with less or no cellular visibility (Fig. 2(b),(e)). Since our pixel clock is too fast for the SPCM acquisition software, the SPCM software is not synchronized to the imaging system making fluorescence lifetime registration a nontrivial technical problem. Without this capability, blur was reduced by utilizing optical tracking in data collection and removing frames where optical tracking failed. Registration of AOFLIO data will be a critical next step towards analysis of fluorescence lifetimes in individual RPE cells.

Besides the system modifications that occurred between paradigm 1 and 2 including the addition of custom splitter electronics to account for LCA variations between subjects, there are other improvements that may make the RPE structure repeatably visible in AOFLIO intensity. To reduce the effects of TCA between the 532 nm excitation and 796 nm channel currently used for co-registration of the fluorescence intensity images, the optical quality of the 532 nm reflectance image could be improved. Additionally, investigating the effect of the maximum likelihood estimation algorithm on the binning size needed and the quality of exponential fits has the potential to improve AOFLIO resolution.

In conclusion, we have successfully adapted an AOSLO to perform AOFLIO in the living human eye. *In vivo* fluorescence lifetime measurements of the RPE layer in multiple human subjects with AOFLIO show consistency between subjects and with previous lipofuscin measurements. While several challenges of human imaging were overcome in this project, there is considerable room

for improvement, most notably in developing software to register the AOFLIO data to improve the structural repeatability. Nonetheless, observations of the RPE mosaic in some images show tantalizing lifetime patterns near the cellular scale, potentially indicating inter- and intra-cellular variations.

Disclosures. KP: University of Rochester (P), QY: University of Rochester (P), JJH: University of Rochester (P).

Data availability. Data underlying the results presented in this paper are available in Table S1 in Supplement 1; raw data files are available upon request.

Supplemental document. See Supplement 1 for supporting content.

References

1. R. R. Rando, "The biochemistry of the visual cycle," Chem. Rev. **101**(7), 1881–1896 (2001).
2. O. Strauss, "The retinal pigment epithelium in visual function," Physiol. Rev. **85**(3), 845–881 (2005).
3. M. F. Marmor, "Mechanisms of fluid accumulation in retinal edema," Doc Ophthalmol. **97**(3/4), 239–249 (1999).
4. H. Song, E. A. Rossi, Q. Yang, C. E. Granger, L. R. Latchney, and M. M. Chung, "High-resolution adaptive optics in vivo autofluorescence imaging in Stargardt disease," JAMA Ophthalmol. **137**(6), 603–609 (2019).
5. J. R. Sparrow, M. Marsiglia, R. Allikmets, S. Tsang, W. Lee, T. Duncker, and J. Zernant, "Flecks in recessive stargardt disease: Short-wavelength autofluorescence, near-infrared autofluorescence, and optical coherence tomography," Invest. Ophthalmol. Visual Sci. **56**(8), 5029–5039 (2015).
6. M. A. Maw, B. Kennedy, A. Knight, R. Bridges, K. E. Roth, E. J. Mani, J. K. Mukkadan, D. Nancarrow, J. W. Crabb, and M. J. Denton, "Mutation of the gene encoding cellular retinaldehyde-binding protein in autosomal recessive retinitis pigmentosa," Nat. Genet. **17**(2), 198–200 (1997).
7. S. Gu, D. A. Thompson, C. R. S. Srikimari, B. Lorenz, U. Finckh, A. Nicoletti, K. R. Murthy, M. Rathmann, G. Kumaramanickavel, M. J. Denton, and A. Gal, "Mutations in RPE65 cause autosomal recessive childhood- onset severe retinal dystrophy," Nat. Genet. **17**(4), 498–502 (1997).
8. J. A. Gambril, K. R. Sloan, T. A. Swain, C. Huisingh, A. V. Zarubina, J. D. Messinger, T. Ach, and C. A. Curcio, "Quantifying retinal pigment epithelium dysmorphia and loss of histologic autofluorescence in age-related macular degeneration," Invest. Ophthalmol. Visual Sci. **60**(7), 2481–2493 (2019).
9. S. Schmitz-Valckenberg, M. Pfau, M. Fleckenstein, G. Staurenghi, J. R. Sparrow, A. Bindewald-Wittich, R. F. Spaide, S. Wolf, S. R. Sadda, and F. G. Holz, "Fundus autofluorescence imaging," Prog. Retin. Eye Res. (2020).
10. H. W. Jung, J. Liu, T. Liu, A. George, M. G. Smelkinson, S. Cohen, R. Sharma, O. Schwartz, A. Maminishkis, K. Bharti, C. Cukras, L. A. Huryn, B. P. Brooks, R. Fariss, and J. Tam, "Longitudinal adaptive optics fluorescence microscopy reveals cellular mosaicism in patients," JCI Insight **4**(6), e124904 (2019).
11. E. A. Rossi, P. Rangel-Fonseca, K. Parkins, W. Fischer, L. R. Latchney, M. A. Folwell, D. R. Williams, A. Dubra, and M. M. Chung, "In vivo imaging of retinal pigment epithelium cells in age related macular degeneration," Biomed. Opt. Express **4**(11), 2527–2539 (2013).
12. C. E. Granger, Q. Yang, H. Song, K. Saito, K. Nozato, L. R. Latchney, B. T. Leonard, M. M. Chung, D. R. Williams, and E. A. Rossi, "Human retinal pigment epithelium: In vivo cell morphometry, multispectral autofluorescence, and relationship to cone mosaic," Invest. Ophthalmol. Visual Sci. **59**(15), 5705–5716 (2018).
13. J. I. W. Morgan, A. Dubra, R. Wolfe, W. H. Merigan, and D. R. Williams, "In vivo autofluorescence imaging of the human and macaque retinal pigment epithelial cell mosaic," Invest. Ophthalmol. Visual Sci. **50**(3), 1350–1359 (2009).
14. T. Ach, C. Huisingh, G. McGwin, J. D. Messinger, T. Zhang, M. J. Bentley, D. B. Gutierrez, Z. Ablonczy, R. T. Smith, K. R. Sloan, and C. A. Curcio, "Quantitative autofluorescence and cell density maps of the human retinal pigment epithelium," Invest. Ophthalmol. Visual Sci. **55**(8), 4832–4841 (2014).
15. G. L. Wing, G. C. Blanchard, and J. J. Weiter, "The topography and age relationship of lipofuscin concentration in the retinal pigment epithelium," Invest. Ophthalmol. Visual Sci. **17**, 601–607 (1978).
16. L. Feeney, "Lipufuscin and melanin of human retinal pigment epithelium," Invest. Ophthalmol. **17**, 583–600 (1978).
17. C. J. Kennedy, P. E. Rakoczy, and I. J. Constable, "Lipofuscin of the retinal pigment epithelium," Atlas of Fundus Autofluorescence Imaging **9**, 763–771 (1995).
18. R. T. Smith, N. L. Gomes, G. Barile, M. Busuioc, N. Lee, and A. Laine, "Lipofuscin and autofluorescence metrics in progressive STGD," Invest. Ophthalmol. Visual Sci. **50**(8), 3907–3914 (2009).
19. J. Sparrow and T. Duncker, "Fundus autofluorescence and RPE lipofuscin in age-related macular degeneration," J. Clin. Med. **3**(4), 1302–1321 (2014).

20. J. R. Sparrow and M. Boulton, "RPE lipofuscin and its role in retinal pathobiology," Exp. Eye Res. **80**(5), 595–606 (2005).

21. C. A. Curcio, "Antecedents of soft drusen, the specific deposits of age-related macular degeneration, in the biology of human macula," Invest. Ophthalmol. Visual Sci. **59**(4), AMD182 (2018).

22. J. P. Greenberg, T. Duncker, R. L. Woods, R. T. Smith, J. R. Sparrow, and F. C. Delori, "Quantitative fundus autofluorescence in healthy eyes," Invest. Ophthalmol. Visual Sci. **54**(8), 5684–5693 (2013).

23. J. R. Lakowicz, *Principles of Fluorescence Spectroscopy*, 3rd ed. (Springer, 2007).

24. M. Y. Berezin and S. Achilefu, "Fluorescence lifetime measurements and biological imaging," Chem. Rev. **110**(5), 2641–2684 (2010).

25. M. A. Digman, V. R. Caiolfa, M. Zamai, and E. Gratton, "The phasor approach to fluorescence lifetime imaging analysis," Biophys. J. **94**(2), L14–L16 (2008).

26. R. Datta, T. M. Heaster, J. T. Sharick, A. A. Gillette, and M. C. Skala, "Fluorescence lifetime imaging microscopy: fundamentals and advances in instrumentation, analysis, and applications," J. Biomed. Opt. **25**(07), 1 (2020).

27. G. Yellen and R. Mongeon, "Quantitative two-photon imaging of fluorescent biosensors," Curr. Opin. Chem. Biol. **27**, 24–30 (2015).

28. L. Goerdt, L. Sauer, A. S. Vitale, N. K. Modersitzki, M. Fleckenstein, and P. S. Bernstein, "Comparing fluorescence lifetime imaging ophthalmoscopy in atrophic areas of retina diseases," Transl. Vis. Sci. Technol. **10**(7), 11–15 (2021).

29. L. Sauer, K. M. Anderson, C. Dysli, M. S. Zinkernagel, P. S. Bernstein, and M. Hammer, "Review of clinical approaches in fluorescence lifetime imaging ophthalmoscopy," J. Biomed. Opt. **23**(09), 1 (2018).

30. L. Sauer, R. H. Gensure, K. M. Andersen, L. Kreilkamp, G. S. Hageman, M. Hammer, and P. S. Bernstein, "Patterns of fundus autofluorescence lifetimes in eyes of individuals with nonexudative age-related macular degeneration," Invest. Ophthalmol. Visual Sci. **59**(4), AMD65–AMD77 (2018).

31. C. Dysli, K. Schürch, E. Pascal, S. Wolf, and M. S. Zinkernagel, "Fundus autofluorescence lifetime patterns in retinitis pigmentosa," Invest. Ophthalmol. Visual Sci. **59**(5), 1769–1778 (2018).

32. C. Dysli, S. Wolf, M. Y. Berezin, L. Sauer, M. Hammer, and M. S. Zinkernagel, "Fluorescence lifetime imaging ophthalmoscopy," Prog. Retinal Eye Res. **60**, 120–143 (2017).

33. L. Sauer, A. S. Vitale, N. K. Modersitzki, and P. S. Bernstein, "Fluorescence lifetime imaging ophthalmoscopy: autofluorescence imaging and beyond," Eye **35**(1), 93–109 (2021).

34. L. Sauer, D. Schweitzer, L. Ramm, R. Augsten, M. Hammer, and S. Peters, "Impact of macular pigment on fundus autofluorescence lifetimes," Invest. Ophthalmol. Visual Sci. **56**(8), 4668–4679 (2015).

35. D. Schweitzer, L. Deutsch, M. Klemm, S. Jentsch, M. Hammer, S. Peters, J. Haueisen, U. A. Müller, and J. Dawczynski, "Fluorescence lifetime imaging ophthalmoscopy in type 2 diabetic patients who have no signs of diabetic retinopathy," J. Biomed. Opt. **20**(6), 061106 (2015).

36. C. Dysli, R. Fink, S. Wolf, and M. S. Zinkernagel, "Fluorescence lifetimes of drusen in age-related macular degeneration," Invest. Ophthalmol. Visual Sci. **58**(11), 4856–4862 (2017).

37. J. A. Feeks and J. J. Hunter, "Adaptive optics two-photon excited fluorescence lifetime imaging ophthalmoscopy of exogenous fluorophores in mice," Biomed. Opt. Express **8**(5), 2483–2495 (2017).

38. S. Walters, J. A. Feeks, K. T. Huynh, and J. J. Hunter, "Adaptive optics fluorescence lifetime imaging ophthalmoscopy of photoreceptors and retinal pigment epithelium in the living non-human primate eye," Biomed. Opt. Express **13**(1), 389 (2022).

39. D. M. Snodderly, J. D. Auran, and F. C. Delori, "The macular pigment. II. Spatial distribution in primate retinas," Invest. Ophthalmol. Vis. Sci. **25**, 674–685 (1984).

40. J. J. Weiter, F. C. Delori, G. L. Wing, and K. A. Fitch, "Retinal pigment epithelial lipofuscin and melanin and choroidal melanin in human eyes," Invest. Ophthalmol. Visual Sci. **27**, 145–152 (1986).

41. A. Dubra and Y. Sulai, "Reflective afocal broadband adaptive optics scanning ophthalmoscope," Biomed. Opt. Express **2**(6), 1757 (2011).

42. Q. Yang, L. Yin, K. Nozato, J. Zhang, K. Saito, W. H. Merigan, D. R. Williams, and E. A. Rossi, "Calibration-free sinusoidal rectification and uniform retinal irradiance in scanning light ophthalmoscopy," Opt. Lett. **40**(1), 85–88 (2015).

43. J. Zhang, Q. Yang, K. Saito, K. Nozato, D. R. Williams, and E. A. Rossi, "An adaptive optics imaging system designed for clinical use," Biomed. Opt. Express **6**(6), 2120–2137 (2015).

44. Q. Yang, J. Zhang, K. Nozato, K. Saito, D. R. Williams, A. Roorda, and E. A. Rossi, "Closed-loop optical stabilization and digital image registration in adaptive optics scanning light ophthalmoscopy," Biomed. Opt. Express **5**(9), 3174–3191 (2014).

45. D. Schweitzer, S. Schenke, M. Hammer, F. Schweitzer, S. Jentsch, E. Birckner, W. Becker, and A. Bergmann, "Towards metabolic mapping of the human retina," Microsc. Res. Tech. **70**(5), 410–419 (2007).

46. F. Docchio, M. Boulton, R. Cubeddu, R. Ramponi, and P. D. Barker, "Age-related changes in the fluorescence of melanin and lipofuscin granules of the retinal pigment epithelium: a time-resolved fluorescence spectroscopy study," Photochem. Photobiol. **54**(2), 247–253 (1991).

47. M. Hammer, L. Sauer, M. Klemm, S. Peters, R. Schultz, and J. Haueisen, "Fundus autofluorescence beyond lipofuscin: lesson learned from ex vivo fluorescence lifetime imaging in porcine eyes," Biomed. Opt. Express **9**(7), 3078–3091 (2018).

48. Q. Yang, H. Song, C. E. Granger, K. Nozato, K. Saito, J. Zhang, L. R. Latchney, M. M. Chung, D. R. Williams, and E. A. Rossi, "Safe real-time imaging of human retinal pigment epithelial cells in the living eye," Invest. Ophthalmol. Vis. Sci. **56**, 5971 (2015).

49. W. Becker, *The Bh TCSPC Handbook*, 6th ed. (2014).

50. A. J. Walsh, J. T. Sharick, M. C. Skala, and H. T. Beier, "Temporal binning of time-correlated single photon counting data improves exponential decay fits and imaging speed," Biomed. Opt. Express **7**(4), 1385 (2016).

51. J. R. Sparrow, Y. Wu, T. Nagasaki, K. D. Yoon, K. Yamamoto, and J. Zhou, "Fundus autofluorescence and the bisretinoids of retina," Photochem. Photobiol. Sci. **9**(11), 1480–1489 (2010).

52. A. N. S. Institute, "American National Standard for Safe Use of Lasers," ANSI Orlando (F, (2014).

53. J. I. W. Morgan, J. J. Hunter, W. H. Merigan, and D. R. Williams, "The reduction of retinal autofluorescence caused by light exposure," Invest. Ophthalmol. Visual Sci. **50**(12), 6015–6022 (2009).

54. J. I. W. Morgan, J. J. Hunter, B. Masella, R. Wolfe, D. C. Gray, W. H. Merigan, F. C. Delori, and D. R. Williams, "Light-induced retinal changes observed with high-resolution autofluorescence imaging of the retinal pigment epithelium," Invest. Ophthalmol. Visual Sci. **49**(8), 3715–3729 (2008).

55. B. D. Masella, D. R. Williams, W. S. Fischer, E. A. Rossi, and J. J. Hunter, "Long-term reduction in infrared autofluorescence caused by infrared light below the maximum permissible exposure," Invest. Ophthalmol. Visual Sci. **55**(6), 3929–3938 (2014).

56. C. Dysli, G. Quellec, M. Abegg, M. N. Menke, U. Wolf-Schnurrbusch, J. Kowal, J. Blatz, O. La Schiazza, A. B. Leichtle, S. Wolf, and M. S. Zinkernagel, "Quantitative analysis of fluorescence lifetime measurements of the macula using the fluorescence lifetime imaging ophthalmoscope in healthy subjects," Invest. Ophthalmol. Visual Sci. **55**(4), 2106–2113 (2014).

57. S. Peters, M. Hammer, and D. Schweitzer, "Two-photon excited fluorescence microscopy application for ex vivo investigation of ocular fundus samples," Adv. Microsc. Tech. II **8086**, 1–10 (2011).

58. A. Hutfilz, S. R. Sonntag, B. Lewke, D. Theisen-Kunde, S. Grisanti, R. Brinkmann, and Y. Miura, "Fluorescence lifetime imaging ophthalmoscopy of the retinal pigment epithelium during wound healing after laser irradiation," Trans. Vis. Sci. Tech. **8**(5), 12 (2019).

59. D. Schweitzer, E. R. Gaillard, J. Dillon, R. F. Mullins, S. Russell, B. Hoffmann, S. Peters, M. Hammer, and C. Biskup, "Time-resolved autofluorescence imaging of human donor retina tissue from donors with significant extramacular drusen," Invest. Ophthalmol. Visual Sci. **53**(7), 3376–3386 (2012).

60. L. Sauer, A. S. Vitale, C. M. Milliken, N. K. Modersitzki, J. D. Blount, and P. S. Bernstein, "Autofluorescence lifetimes measured with fluorescence lifetime imaging ophthalmoscopy (FLIO) are affected by age, but not by pigmentation or gender," Trans. Vis. Sci. Tech. **9**(9), 2–13 (2020).